

Screening of House Dust from Chinese Homes for Chemicals with Liver X Receptors Binding Activities and Characterization of Atherosclerotic Activity Using an *in Vitro* Macrophage Cell Line and ApoE^{−/−} Mice

Wenxin Hu,¹ Yingting Jia,¹ Qiyue Kang,¹ Hui Peng,² Haojia Ma,¹ Shiyi Zhang,¹ Youhei Hiromori,^{3,4} Tomoki Kimura,⁵ Tsuyoshi Nakanishi,³ Lemin Zheng,⁶ Yifu Qiu,⁷ Zhaobin Zhang,¹ Yi Wan,¹ and Jianying Hu¹

¹Laboratory for Earth Surface Processes, College of Urban and Environmental Sciences, Peking University, Beijing, China

²Department of Chemistry, University of Toronto, Toronto, Ontario, Canada

³Laboratory of Hygienic Chemistry and Molecular Toxicology, Gifu Pharmaceutical University, Gifu, Gifu, Japan

⁴Faculty of Pharmaceutical Sciences, Suzuka University of Medical Science, Suzuka, Mie, Japan

⁵Department of Life Science, Faculty of Science and Engineering, Setsunan University, Ikedanakamachi, Neyagawa, Japan

⁶School of Basic Medical Sciences, Peking University Health Science Center, Peking University, Beijing, China

⁷Institute of Molecular Medicine, Peking University, Beijing, China

BACKGROUND: Atherosclerotic cardiovascular disease has become the leading cause of death worldwide, and environmental pollutants are increasingly recognized as risk factors for atherosclerosis. Liver X receptors (LXRs) play a central role in atherosclerosis; however, LXR activity of organic pollutants and associated potential risk of atherosclerosis have not yet been characterized.

OBJECTIVES: This study aimed to explore whether LXR-antagonistic chemicals are present in indoor house dust and, if so, to characterize this activity in relation to changes in macrophages *in vitro* and cardiovascular disease indicators *in vivo* in an atherosclerosis ApoE^{−/−} mouse model.

METHODS: We used a His-LXR α -pull-down assay and a nontarget high-resolution mass spectrometry method to screen house dust collected from Chinese homes for LXR α - and LXR β -antagonist activity. A chemical identified in this manner was assessed for its ability to induce cholesterol efflux and foam cell formation in RAW264.7 macrophages, to down-regulate the expression of two LXR-dependent genes, *ABCA1* and *ABCG1*, and finally to induce atherosclerotic lesions *in vivo* using an ApoE^{−/−} mouse model.

RESULTS: We identified the flame retardants triphenyl phosphate (TPHP) and 2-ethylhexyl diphenyl phosphate (EHDP) in house dust samples and demonstrated their ability to antagonize LXRs. The potency of TPHP was similar to that of the LXR-antagonist SR9238. TPHP could also inhibit cholesterol efflux and promote foam cell formation in RAW264.7 macrophages and mouse peritoneal macrophages and significantly promoted atherosclerotic lesion formation in the ApoE^{−/−} mouse model.

CONCLUSIONS: We found LXR-antagonist chemicals in environmental samples of indoor dust from Chinese homes. One of the chemicals, TPHP, was able to promote the development of atherosclerotic lesions in the ApoE^{−/−} mouse model. These results highlight the need to assess the LXR-antagonist activities of pollutants in future environmental management programs. <https://doi.org/10.1289/EHP5039>

Introduction

The incidence of cardiovascular disease (CVD) has increased in many countries, and CVD has been the leading underlying cause of death worldwide since 2000 (WHO 2018). CVD contributed to one in every three deaths in the United States in 2008 (Roger et al. 2012) and to two in every five deaths in China in 2014 (Chen et al. 2017). More than 80% of CVD can be attributed to modifiable and nongenetic factors, and lifestyle choices such as smoking, diet, and exercise were considered as major environmental influences on CVD (Bhatnagar 2006). Recent disparate lines of evidences together indicate that exposure to chemical pollutants plays a larger role in the etiology of CVD than previously thought (Bhatnagar 2004). The adverse effects of fine particles present in ambient air and metal on CVD have been demonstrated in epidemiological and animal studies (Bhatnagar 2004, 2006; Brook et al. 2004). However, significant gaps remain

in our understanding of the environmental factors that affect cardiovascular health (Bergman et al. 2013).

Atherosclerosis is a major cause of CVD. Foam cell (i.e., cholesterol-laden macrophages) formation within the artery wall can facilitate adventitia angiogenesis and the buildup of necrotic pools, thereby playing a key role in atherosclerosis pathogenesis (Tontonoz and Mangelsdorf 2003). Liver X receptors (LXRs, including the LXR α and LXR β subtypes) regulate foam cell formation by functioning as cholesterol sensors that regulate cholesterol efflux to achieve a balance between cholesterol influx and efflux in foam cells (Glass and Witztum 2001; Pennings et al. 2006; Yu et al. 2013). Recent studies showed that treatment of atherosclerotic mice with a synthetic LXR agonist (GW3965) inhibited foam cell formation and promoted regression of atherosclerotic plaques (Joseph et al. 2002) and that macrophage-specific deletion of LXRs in mice enhanced atherosclerosis (Tangirala et al. 2002). Due to the central role played by LXRs in atherosclerosis pathogenesis, chemicals that can activate LXRs have been designed as drugs to treat atherosclerosis (Joseph et al. 2002; Terasaka et al. 2003). Thus, it is possible that pollutants with LXR-antagonist activities may induce atherosclerosis by promoting foam cell formation. These findings led us to postulate that human exposure to pollutants with LXR-antagonist activities would induce atherosclerosis by promoting foam cell formation.

To test this hypothesis, this study was designed to determine *a*) whether LXR-antagonist chemicals are present in indoor dust (a well-known carrier of various pollutants and human exposure matrix) (Suzuki et al. 2013; Kassotis et al. 2017; Fang et al. 2015), and *b*) whether these LXR-antagonist environmental chemicals can promote foam cell formation and consequently induce atherosclerosis in an experimental animal model.

Address correspondence to Jianying Hu, Laboratory for Earth Surface Processes, College of Urban and Environmental Sciences, Peking University, Beijing 10087 China. Telephone: 86-10-62765520. Email: Hujy@urban.pku.edu.cn

Supplemental Material is available online (<https://doi.org/10.1289/EHP5039>). The authors declare they have no actual or potential competing financial interests.

Received 14 January 2019; Revised 21 October 2019; Accepted 23 October 2019; Published 14 November 2019.

Note to readers with disabilities: EHP strives to ensure that all journal content is accessible to all readers. However, some figures and Supplemental Material published in EHP articles may not conform to 508 standards due to the complexity of the information being presented. If you need assistance accessing journal content, please contact ehponline@niehs.nih.gov. Our staff will work with you to assess and meet your accessibility needs within 3 working days.

Materials and Methods

Chemicals and Reagents

The names and sources of chemicals and reagents used in the study are listed in Table S1. Dose solutions of SR9238, triphenyl phosphate (TPHP), *p*-nitrophenol (PNP), and 2-ethylhexyl diphenyl phosphate (EHDPP) were prepared in dimethyl sulfoxide (DMSO) on the basis of their molarity.

Indoor Dust Sample Collection and Extraction

The indoor dust used in this study was collected using brooms from the main living area (floor and the top of furniture) of 29 Chinese homes. To prevent contamination between different households, a new broom was used for sample collection from each household. The sampling locations were chosen based on convenience. As shown in Table S2, samples were obtained from cities in various regions of China including Beijing, Yiyang, Zhengzhou, Fuzhou Shanghai, Guangzhou, and Chongqing. The homes varied in age and size and were inhabited by persons of varying incomes (see Table S2). For example, the monthly income of the family ranged from <5,000 to 20,000 RMB, the size of the house ranged from ~20 to 185 m², the age of the house ranged from <5 to 10–30 y, the age of the furniture ranged from <5 to 10–30 y, and the distance from the house to the nearest road ranged from ~20 to 800 m. A dust standard reference material (SRM2585) was purchased from the National Institute of Standards and Technology. The indoor dust was collected, wrapped in aluminum foil, and stored at –20°C until extraction. As much as possible, impurities (clips, small stones, human and animal hair, and wood chips) were removed from the dust sample by using tweezers. The dust samples were then extracted as described previously (Fang et al. 2015). In brief, 0.1 g of a dust sample was extracted with 5 mL acetone/hexane (1:1, vol/vol), followed by shaking for 20 min on an orbital shaker and then sonicating for 15 min. After centrifugation at 4,000 rpm for 10 min, the acetone/hexane extract was transferred to a clean glass bottle. The residue was subjected to extraction twice, and the organic solvent extracts were combined. The 7.5-mL extracts were evaporated to near dryness under a gentle stream of high purity nitrogen and reconstituted in 7.5 mL methanol (MeOH) for determining the concentrations of TPHP and EHDPP. The residual extracts of 7.5 mL were evaporated to near dryness and reconstituted in 200 μ L DMSO to form a 500-mg dust/mL DMSO solution for the yeast two-hybrid assay. A 10- μ L aliquot of the DMSO solution from 11 samples (Samples 1–11; listed in Table S2) was then composited to create a mixture sample for screening the indoor dust for LXR ligands. Glass tubes used during the extraction process were pretreated at 500°C for 6 h to prevent background contaminations. The sample collection was approved by the ethics committee of Peking University, and informed consent was obtained from each homeowner.

Screening LXR Ligands Using a Pull-Down Assay and a Nontarget Chemical Analysis

In the pull-down assay, the full-length human LXR α gene was amplified by polymerase chain reaction (PCR) using KOD FX Neo DNA polymerase A plasmid vector pCMX-hLXR α , kindly provided by Dr. D. Mangelsdorf from the University of Texas Southwestern Medical Center, was used as a template. After preincubation at 94°C for 2 min, PCR was performed with 40 cycles of 98°C (10 s), 58°C (30 s), and 72°C (60 s). Primers used were as follows:

forward 5'-GCTCGGTACCCTCGAAATGTCCTTGTGGC-TGGG-3'

reverse 5'-ATTCGGATCCCTCGATCATTCGTGCACATC-CCAG-3'.

The amplified circular DNA (cDNA) was subcloned into the pCold-trigger factor (TF) vector predigested with EcoRI using the In-Fusion HD Cloning Kit according to the manufacturer's instructions. In brief, the 50 ng of predigested plasmid and the 100 ng of amplified cDNA were mixed with 2 μ L premix solution (In-Fusion HD Cloning Kit), and then the mixture was adjusted to 10 μ L using double-distilled water. After incubation at 50°C for 15 min, the reaction mixture was transformed into *Escherichia coli* (*E. coli*) DH5 α -competent cells by heat shock transformation (the mixture was incubated on ice for 30 min, at 42°C for 90 s, and then transferred to ice for another 3 min). The expression plasmids of pCold-His-TF-LXR α or pCold-His-TF were transfected into *E. coli* BL21 cells by heat shock transformation. The expression of His-TF or His-TF-LXR α was induced with 0.4 mM isopropyl β -D thiogalactoside at 20°C for 18 h. The recombinant proteins were purified with a nickel-affinity column (Ni²⁺-charged HiTrap chelating high-performance column from GE Healthcare), followed by a Hitrap desalting (GE Healthcare) to remove imidazole. The expression of His-TF-LXR α was detected by sodium dodecyl sulfate-polyacrylamide gel electrophoresis (SDS-PAGE) (see Figure S1A) with 4% stacking and 15% resolving, and the gel was stained with Coomassie® blue (Imperial Chemical). For the pull-down assay, 20 μ M His-TF-LXR α (n = 6) and 20 μ M His-TF (n = 6) was spiked with 5 μ L of house dust extract and incubated in 2-mL glass tubes at 4°C for 1 h. After adding 100 μ L of His-select nickel magnetic agarose beads (Beaver Life Science) to each tube, the mixture was incubated for 2 h in a shaker at approximately 170 rpm at 4°C. After removing the supernatant using a magnetic separator, the residues were washed twice with 1 mL buffer (20 mM Tris and 20 mM NaCl; pH 8.0), and LXR α protein was then eluted from the His-select nickel magnetic agarose beads with 1 mL buffer (20 mM Tris, 500 mM NaCl, and 250 mM imidazole; pH 8.0). This protein elution step was performed in triplicate. The chemicals bound to the LXR α protein were extracted by adding ethyl acetate (7 mL) and formic acid (FA; 60 μ L), followed by shaking on an orbital shaker for 15 min and centrifuging at 4,000 rpm for 5 min. The extracts were concentrated to near dryness under a gentle stream of high-purity nitrogen and reconstituted in MeOH for nontarget chemical analysis. A negative control experiment was performed using the same protocol but with His-TF protein instead of His-TF-LXR α protein. We used freshly purified LXR α protein to pull down LXR ligands from the indoor dust extracts. The efficiency of the recombinant LXR α to pull down chemicals was confirmed using the positive LXR α ligand TO901317 at 0.25-, 2.5-, 25-, and 250- μ g/L concentrations, and the recoveries of TO901317 were 100% \pm 3%, 85% \pm 5%, 80% \pm 0.7%, and 92% \pm 4%, respectively (see Figure S1B). The average percentage of pulled down TO901317 of the spiked concentration in the His-TF-LXR α group was 89%, and the average percentage of pulled down TO901317 of the spiked concentration in the control group was 10% (see Figure S1C).

A Dionex UltiMate 3000 Ultra high-performance liquid chromatography–quaternary (UHPLC-Q)-Exactive™ mass spectrometer (MS) system (Thermo Fisher Scientific) was used for the nontargeted chemical analysis. Separation of chemicals was achieved by use of a C18 column (1.7 μ m, 2.1 mm \times 100 mm; Waters). Milli-Q® water (A phase) and MeOH (B phase) were employed as the mobile phases. In 0–3 min, the B phase increased from 5% to 60%. Then in 3–13 min, the B phase increased from 60% to 100%, and was held static for 3 min. Finally the B phase fell back to the initial condition, which was held for 4 min for equilibration. The sample injection volume, flow rate, column temperature, and sample compartment temperature were set to 5 μ L, 0.30 mL/min,

40°C, and 5°C, respectively. In the mode of full scan MS/data-dependent (dd) MS2, the full scan resolution was set at 70,000, and the ddMS2 resolution was set at 17,500. In the full scan and ddMS2, the automatic gain control values were 3×10^6 and 5×10^4 , and maximum injection time values were set at 100 ms and 80 ms, respectively. The isolation window of precursor ions was set to 1.0 m/z. The TopN was set to 5, where N represents the top most abundant product ions. The step-normalized collision energy was set to 10, 30, and 50. The parameters for electrospray ionization mode were set as follows: the spray voltages of 3 kV and 3.5 kV were for negative and positive modes, respectively; the capillary temperature was maintained at 320°C; and the sheath gas flow and auxiliary gas flow were set to 35 Arb and 10 Arb, respectively. The S-lens radio frequency (rf) level was 50.

The data sets were deconvoluted and aligned using Progenesis[®] QI (Waters). The initial and final retention times were set at 2 and 16.2 min, respectively, and peaks with 5,000 minimum intensity in the negative mode and 10,000 minimum intensity in the positive mode were used for further analysis. Adducts considered in this experiment included $[M-H_2O-H]^-$, $[M-H]^-$, $[M+Cl]^-$, and $[M+FA-H]^-$ in the negative mode and $[M+H-H_2O]^+$, $[M+H]^+$, $[M+NH_4]^+$, $[M+Na]^+$, and $[M+K]^+$ in the positive mode. To differentiate the chemicals between the His-TF-LXR α and control groups, principal component analysis (PCA) was performed based on the aligned peak list using SIMCA-P+ (version 12.0; Umetrics). The fold change for each feature matched across samples was calculated as the ratio of the area of each peak in the His-TF-LXR α group to the area of each peak in the control group. Peaks with a fold change of >3 ($p < 0.05$ with Student's *t*-test) in the His-TF-LXR α group compared with the fold change in the control group were considered as potential ligands of LXR α . These chemicals were manually checked using formula exact mass and retention time. Formulas were further calculated by use of Progenesis[®] QI based on the extract mass at the mass error of 5 ppm, element numbers of $C_{50}H_{200}N_{10}O_{10}P_5S_5Cl_{10}Br_{10}F_{10}$, and the isotopic difference of $<10\%$. Then the database of mzCloud (<https://www.mzcloud.org/>), which provides accurate mass spectra based on high resolution mass spectrometry (HRMS), was used to identify the structures of the LXR ligands in the indoor dust samples, the mass tolerance was set to 5 ppm, and peaks with MS/MS spectra containing at least two product ions matched with the database were selected for further evaluation. The standards of TPHP, EHDPP, and PNP (see Table S1) were purchased for obtaining their mass spectra and the chromatograms that were compared with those of the dust samples to ultimately confirm their structures.

To determine the concentrations of TPHP and EHDPP in the indoor dust extracts, the UHPLC-Q Exactive[™] MS was operated in positive ionization mode, and the instrumental method was the same as the nontarget chemical analysis. As an internal standard, TPHP-*d*₁₅ was added to the indoor dust extracts at 5 ng/mL. Linearity was valid between 0.1 and 100 ng/mL, and regression coefficients of 7-point standard curves were always >0.99 . Because low levels of TPHP and EHDPP were detectable in blank samples, the limit of detection of TPHP and EHDPP were set as the average blank signal plus three times the standard deviation (SD) (0.05 ng/mL for TPHP and 0.01 ng/mL for EHDPP). The contribution was calculated as the ratio of the concentration determined by the instrumental method and the concentration equivalent to the inhibition based on *in vitro* bioassay. As described previously (Villeneuve et al. 2000), the equivalent concentration was calculated by a single-point estimation at the maximum dust dose (500 μ g indoor dust/mL) when the inhibition of a sample was less than 20%, otherwise the multiple-point estimation method was used to derivate the TPHP equivalent concentration by fitting a regression model to the dose-response relationship.

Assessment of LXR Activity

The LXR-agonistic and -antagonistic activities of the indoor dust samples and identified chemicals were assessed by a yeast two-hybrid assay using human LXRs and coactivator transcription intermediary factor 2 in *Saccharomyces cerevisiae* Y187. The yeast expression plasmids, pGBT9 and pGAD424, were purchased from Clontech/Takara-Bio. The ligand-binding domains (LBDs) of LXR α (residues 205–447) and LXR β (residues 219–460) and the receptor interaction domains (RIDs) of transcriptional intermediary factor 2 (TIF2) (residues 483–1,090) were amplified from human total RNA (Clontech/Takara-Bio) by reverse transcription (RT)-PCR. The following primers used were designed and purchased from Sigma-Aldrich: LXR α LBD: forward 5'-CGGAGGAGTGTGTCCTGTCAGA-3', reverse 5'-TCATTCTG-TGACGCCCAGATCTC-3'; LXR β LBD: forward 5'-AGGG-AGCAGGCTCCTTTCTGAA-3', reverse 5'-TCACTCGTGGA-CGCCAGATCTC-3'; TIF2 RID: forward 5'-TCCGAATCC-CACCCAGTCAG-3', reverse 5'-TAAGGCTCTATCAATCT-CCTCCAG-3'. The RT-PCR was performed by AmpliTaq Gold[®] DNA polymerase (Thermo Fisher Scientific) as follows: LXR α LBD and LXR β LBD: 95°C for 5 min, 35 cycles of denaturation at 95°C for 15 s, 60°C for 15 s, and 72°C for 60 s; TIF2 RID: 95°C for 5 min, 35 cycles of denaturation at 95°C for 15 s, 58°C for 15 s, and 72°C for 120 s. The amplified LXR α LBD or LXR β LBD and the TIF2 RID fragments were subcloned into pGBT9 digested with SmaI-BamHI (Takara Bio) and pGAD424 digested with EcoRI-BamHI (Takara Bio), respectively. The ligation reaction was performed using T4 DNA ligase with a DNA ligation kit (Takara Bio) by incubating at 16°C for 1 h. The yeast expression plasmids for fusion protein of GAL4 DNA-binding domain (DBD)—LXR-LBD (pGBT9-LXR α and pGBT9-LXR β) consisted of LXR-LBD residues coupled to the GAL4 DBD in pGBT9. The yeast expression plasmid for fusion protein of GAL4 activation domain (AD)—TIF2 RID (pGAD-TIF2) consisted of the TIF2-RID residues coupled to the GAL4 AD in pGAD424. Yeast cells were transformed by the lithium acetate (LiAc) method. In brief, yeast cells were precultured in yeast extract peptone dextrose (YPDA) medium (Clontech/Takara-Bio). At 18 h after preculture, yeast cells were grown to optical density (OD)₅₉₅ = 0.4–0.6. The cells were resuspended in a polyethylene glycol (PEG) LiAc solution (0.1 M LiAc, 40% wt/vol PEG 4000, 10 mM Tris-HCl, 1 mM EDTA; pH 7.5) and incubated at 30°C for 30 min. Then the cells were transfected with pGBT9-LXR α (or pGBT9-LXR β) and pGAD-TIF2 by heat shock (42°C for 15 min). After heat shock, the cells were centrifuged at 3,000 rpm for 3 min at room temperature. The centrifuged cells were resuspended in distilled water, and then were centrifuged at 3,000 rpm for 3 min at room temperature. The centrifuged cells were then resuspended in a LiAc solution (0.1 M LiAc, 10 mM Tris-HCl, 1 mM EDTA; pH 7.5) and plated onto the agar plate. The transfected cells were selected on synthetic defined (SD) minimal medium (for details, see Table S3) solidified with agar at 30°C for 2–3 d. The yeast two-hybrid experiment was carried out as described previously (Zhang et al. 2015). Briefly, transformed yeast cells were cultured (~ 15 h, 30°C, with shaking) in SD medium (for details, see Table S3). After the cell suspension (50 μ L) and chemicals or house dust extracts (2.5 μ L, in DMSO) were added to the SD medium (200 μ L), the culture mixtures were incubated at 30°C for 4 h with shaking. Then the culture mixtures (150 μ L) were removed for determining the absorbance at 595 nm by a microplate reader (Thermo Fisher Scientific). The residual cells were lysed with 200 μ L Z buffer (for details, see Table S3). After incubation at 30°C for 20 min, 40 μ L of 2-nitrophenyl-b-D-galactoside (4 mg/mL) was added and reacted at 30°C for 30 min. The reaction was terminated by adding 100 μ L sodium carbonate (1 M). Finally, the mixtures (150 μ L) were added into a

96-well microplate for detecting the absorbance at 415 and 570 nm. Then β -galactosidase activity was calculated by Equation 1:

$$\beta\text{-galactosidase activity} = (OD_{415} - 1.75 \times OD_{570}) / (OD_{595}) \quad (1)$$

where OD_{595} , OD_{415} , and OD_{570} represent the absorbance at 595, 415, and 570 nm, respectively. DMSO (1%) was used as the control. The LXR agonist TO901317 and the LXR antagonist SR9238 were used as positive controls. The stock solution of TO901317 was diluted by a 3-fold serial dilution with DMSO, and 11 concentrations (0.05–3,000 nM) were prepared ($n = 3$ per group). Half-maximal effective concentration (EC_{50}) values were determined to be 100 nM for LXR α and 220 nM for LXR β . The stock solution of SR9238 was diluted by a 2-fold serial dilution with DMSO, and 11 concentrations (24.4–25,000 nM) were prepared ($n = 3$ per group). The half-maximal inhibitory concentration (IC_{50}) values were determined to be 824.7 nM for LXR α and 446.4 nM for LXR β . To determine whether indoor dust extracts possessed LXR agonistic or antagonistic activity, indoor dust extracts were diluted by a 3-fold serial dilution with DMSO, and five various concentrations (6–500 $\mu\text{g/mL}$) were further prepared ($n = 3$ per group). The inhibition (%) was calculated by Equation 2:

$$\text{Inhibition \%} = \left(\frac{[A - B]}{A} \right) \times 100 \quad (2)$$

where A represents the β -galactosidase activity induced by TO901317 at 100 nM for LXR α and 220 nM for LXR β , and B represents the β -galactosidase activity after co-exposing to house dust extract at different concentrations and TO901317 at 100 nM for LXR α and 220 nM for LXR β . To determine whether the identified chemicals possessed LXR-agonistic or -antagonistic activity, standards of TPHP, EHDPP, and PNP were tested. Stock solutions were diluted by a 2-fold serial dilution with DMSO, and 11 various concentrations (24.4–25,000 nM for PNP and 48.8–50,000 nM for TPHP and EHDPP) were further prepared ($n = 3$ per group). To determine whether the identified chemicals possessed LXR-antagonistic activity, TO901317 at EC_{50} (100 nM for LXR α and 220 nM for LXR β) along with the diluted chemicals was added to the medium. The final DMSO concentration was 1% in the medium. The IC_{50} was calculated based on the sigmoidal dose–effect curves using Prism software (version 5; Graphpad Inc.).

Cell Cultures and Treatments

RAW264.7 cells were obtained from the National Infrastructure of Cell Line Resource of Beijing, China, and the cells used for the experiment were cultured for at least three passages. Dulbecco's Modified Eagle's Medium (DMEM)-F12 medium containing 10% fetal bovine serum (FBS) was employed to culture the RAW264.7 cells. RAW264.7 cells were incubated at 37°C with 5% carbon dioxide. The RAW264.7 cells were plated at 2.5×10^5 cells/well (6-well plates), 6.0×10^4 cells/well (24-well plates), and 10^4 cells/well (96-well plates). The RAW264.7 cells were plated and grown overnight; then the medium was removed and fresh DMEM-F12 contained with 0.1% DMSO (control; $n = 3$) or TPHP at the concentrations of 1–20,000 nM ($n = 3$ per group) was added. For the LXRs reactivated experiment, RAW264.7 cells were seeded for 24 h and then the cells were treated simultaneously with TPHP (10,000 nM, $n = 3$) and TO901317 at 5, 10, or 100 nM in DMSO ($n = 3$ per group) or with 0.1% DMSO (control; $n = 3$). Then the cells were used for the quantitative reverse transcription (qRT)-PCR, cellular cholesterol efflux assay, and foam cell formation experiment.

Cell Viability

Cell viability was assessed using the CellTiter-Glo® Luminescent Cell Viability Assay based on the manufacturer's instructions ($n = 3$ per group). Luminescence was assessed using an LB 941 TriStar multimode microplate reader (Berthold Technologies).

Quantitative Reverse Transcription–Polymerase Chain Reaction

Total RNA was isolated from RAW264.7 cells and mouse peritoneal macrophages using TRIzol reagent according to the manufacturer's instructions. Then a Nanovue Plus™ spectrophotometer (GE Healthcare Life Science) was used to analyze the concentration, quality, and purity of the RNA. Total RNA (1 μg) was mixed with oligo deoxythymine (dT) (1 μL) at 70°C for 5 min and then combined with a mixture containing Moloney murine leukemia virus (MMLV) reverse transcriptase (1 μL), deoxy-ribonucleoside triphosphate (dNTP) (1.25 μL), Recombinant RNasin® Ribonuclease Inhibitor (Promega) (0.65 μL), and MMLV buffer (5 μL) at 42°C for 60 min. The SYBR® Green PCR Kit (TOYOBO) was used for RT-PCR analysis. Real-time fluorescence detection was performed using the StepOnePlus™ sequence detection system (Applied Biosystems). Relative gene expression was evaluated by the $2^{-\Delta\Delta Ct}$ method, as suggested by Applied Biosystems. The following primers were designed and purchased from Sangon Biotech:

actin: 5'-CCTGGCACCCAGCACAAT-3' and 5'-GCCGATCCACACACGGAGTACT-3' ATP-binding cassette transporter A1 (ABCA1): 5'-CCCAGAGCAAAAAGGGACTC-3' and 5'-GGTCATCATCACTTTGGTCCTTG-3'

ATP-binding cassette transporter G1 (ABCG1): 5'-CAAGACCCTTTTGAAAGGGATCTC-3' and 5'-GCCAGAATATT-CATGAGTGTGGAC-3'.

Cellular Cholesterol Efflux Assay

RAW264.7 cells or mouse peritoneal macrophages were plated in 96-well plates at 10^4 cells/well and cultured with DMEM-F12 containing 10% FBS and 1 $\mu\text{g/mL}$ 22-[N-(7-nitrobenz-2-oxa-1,3-diazol-4-yl)amino]-23,24-bisnor-5-cholesten-3 β -ol (NBD-cholesterol) for 24 h. Subsequently, the medium was completely removed and fresh DMEM-F12 containing 10% FBS and 0.1% DMSO (control; $n = 3$) or TPHP at the concentration of 1–20,000 nM ($n = 3$ per group) was added. After a further 24-h incubation, the cells were washed with phosphate-buffered saline (PBS) and then incubated with serum-free medium containing ApoA-I (20 $\mu\text{g/mL}$) or high-density lipoprotein (HDL; 50 $\mu\text{g/mL}$) for 4 h. Then the medium was collected, and the cells were lysed with a cell lysis buffer. NBD-cholesterol in the medium and cell lysis buffer were measured, respectively, using a Tecan Infinite® M1000Pro Microplate Reader (Tecan Group Ltd.) at 485-nm excitation wavelength and 535-nm emission wavelength. Cholesterol efflux was expressed as a percentage of fluorescence in the medium relative to the total amount of fluorescence.

Foam Cell Formation

RAW264.7 cells or mouse peritoneal macrophages were plated in 24-well plates at 6.0×10^4 cells/well and grown overnight. Then the medium was removed and fresh DMEM-F12 containing 10% FBS, 20 $\mu\text{g/mL}$ oxidized low-density lipoprotein (ox-LDL), and 0.1% DMSO (control; $n = 3$) or TPHP at the concentration of 1–20,000 nM ($n = 3$ per group) was added. The cells were washed with PBS, followed by fixing in 4% paraformaldehyde for 30 min and staining with boron-dipyrromethene (BODIPY) 493/503 (20 $\mu\text{g/mL}$) and 4',6-diamidino-2-phenylindole (DAPI; 100 ng/mL) for 10 min. Foam cell formation

was analyzed by high-content microscopy using ImageXpress® Micro XL (Molecular Devices). From each well, 25 image fields were scanned, and MetaXpress® (Molecular Devices) was used to quantify compartmentalized changes in the fluorescence of each cell.

Animals and Exposure

All experiments related to animals were approved by the institutional animal care and use committee of Peking University and followed the guidelines for animal experiments of the university as well as for experimental animals in China. The biological effect size of the animal experiments was based on the previous paper (Negro Silva et al. 2017). C57BL/6 (12 weeks old) and ApoE^{-/-} mice (12 weeks old) were obtained from the Beijing Vital River Laboratory Animal Technology Company. Mice used in the experiments were acclimated to the housing unit 2 weeks before they were used for experiments, and they were randomly assigned to control or TPHP treatment groups. Five animals were housed to a cage, and mice were acclimated to the controlled environment (temperature: 22 ± 2°C; relative humidity: 40–60%; artificial lighting: 12 h:12 h light/dark). Mice received diet and drinking water *ad libitum*. Body weight (BW) was measured every week during the dosing period. Forty-five C57BL/6 mice and 27 ApoE^{-/-} mice were used in this study. Animal protocol 1: Male C57BL/6 mice (five mice per group) were fed a basic diet (Laboratory Animal Center of the Academy of Military Medical Sciences, China). On Day 0, mice were stimulated with paraffin oil by intraperitoneal injection. From Day 1 to Day 7, mice were exposed to corn oil (control) or TPHP (dissolved in corn oil) at 40 or 200 mg/kg BW by daily oral gavage. The volume of the corn oil or TPHP in corn oil administered was 5 mL/kg BW. On Day 8, after the mice were anesthetized by sodium pentobarbital via intramuscular injection, peritoneal macrophages were harvested from peritoneal lavage with 4 mL pre-warmed DMEM-F12 (containing 10% FBS) using a 25-gauge needle; 5–10 min later, 3–3.5 mL peritoneal fluid was collected, and the cells were isolated by centrifuge at 1,000 rpm for 5 min. The isolated cells were cultured in DMEM-F12 containing 10% FBS. After 4 h, the medium was changed, and the cells were cultured overnight. The cells were then used for the qRT-PCR, cellular cholesterol efflux assay, and foam cell formation experiment. The exposure period used in the present study was based on previous studies, in which peritoneal macrophages were harvested from mice treated with chemicals for 4–14 d (Li et al. 2009; Saeed et al. 2012). Considering that this study assessed the effects of short-term exposure to TPHP, whereas humans are exposed to TPHP over a lifelong period, the present study used exposure doses that were higher than that of human exposure from house dust. Animal protocol 2: Because wild-type mice are highly resistant to atherosclerosis, a well-established atherosclerosis model, the ApoE^{-/-} mouse, was used in the study. The male ApoE^{-/-} mice (nine mice per group) were fed a high-fat diet (D12108C; Research Diets Inc.) and exposed to corn oil (control) or TPHP (dissolved in corn oil) at 10 or 40 mg/kg BW for 13 weeks by oral gavage. Mice were sacrificed 24 h after the last day of exposure with an overdose of sodium pentobarbital via intraperitoneal injection. Because the formation of atherosclerosis lesions required a long time, the exposure period used in the present study was based on previous studies in which the effects of chemicals on formation of atherosclerosis lesions were observed after an exposure period of 12–15 weeks (Li et al. 2009; Negro Silva et al. 2017; Shi et al. 2016). The doses of TPHP used in the ApoE^{-/-} model mouse referred to previous studies in which mice were treated with TPHP at 50–300 mg/kg BW to observe significant adverse effects, including decreased testosterone levels and hypertriglyceridemia

(Chen et al. 2015; Morris et al. 2014). Although the adverse effects were observed in mice exposed to a higher dose than the human exposure dose in those studies, epidemiological studies have associated TPHP exposure with decreased sperm concentration and hypertriglyceridemia (Meeker and Stapleton 2010; Zhao et al. 2019).

Plasma Lipids and Atherosclerotic Lesion Analysis

Treated ApoE^{-/-} mice ($n = 9$ per group) were fasted overnight, and heart puncture was used to collect the blood soon after each animal was sacrificed. The blood samples were then centrifuged (1,000 × g , 10 min, 4°C) to separate the plasma, and the plasma was stored at –80°C. The total cholesterol (TC), triglyceride (TG), low-density lipoprotein cholesterol (LDL-C), and high-density lipoprotein cholesterol (HDL-C) levels in the plasma were measured using Roche Diagnostics COBAS MIRA, following the manufacturer's instructions. For atherosclerotic lesion analysis, nine mice per group were evaluated. The aortas from the base of the ascending aorta to the iliac bifurcation were separated, and the aortic roots with the heart were harvested. For *en face* aorta analyses, the aortic tree was perfused with PBS, and the aorta was then dissected *en bloc* from the root to the iliac bifurcation by removing minor branching arteries and fat tissue. The aortic lumen was opened with a longitudinal incision and then immediately fixed in 4% paraformaldehyde. After 24 h of fixation, aortic lipids were stained with Oil Red O, and the stained aortas were photographed. The percentage of aortic area stained with Oil Red O was determined using the image analysis software Image J software (Schneider et al. 2012). For histological analysis of the aortic roots, PBS-perfused aortas and hearts were fixed in 4% paraformaldehyde/PBS for 5 h, followed by incubation in 30% sucrose for at least 20 h at 4°C. Hearts were cut in half, and the upper part was embedded in O.C.T. (Coolaber Science & Technology) for the frozen sections. Three serial 6- μ m sections were cut from the point of appearance of the aortic valve leaflets from the frozen hearts, and the sections were stained with Oil Red O. An equal number of aortic valve sites (three slides per mouse) were analyzed in both the corn oil (control) and TPHP-exposed mice. The stained surface area in the sections was quantified using ImageJ software.

Immunofluorescence Staining

Slides (three slides per mouse) loaded with frozen 6- μ m sections were rinsed in PBS, followed by quenching of endogenous peroxidase in 3% hydrogen peroxide for 30 min and permeation by 0.25% Triton™ X-100 in PBS for 20 min. The slides were incubated with blocking reagent (ZSGB-BIO, ZLI-9,022) for 30 min at room temperature. Antigens were then successively detected using the Opal 7-Color IHC Kit (NEL797001KT) according to the manufacturer's instructions. Briefly, slides were incubated with macrophage antibody (MOMA)-2 (Abcam; ab33451, 1:300, Opal 650) and α -Smooth Muscle Actin (SMC α -Actin; CST, 19245, 1:500, Opal 520) for 2 h in a humidified chamber at 37°C, followed by detection using the horseradish peroxidase (HRP)-conjugated secondary antibody (GBI Labs; Polink-1 HRP polymer detection kit) and fluorophore-conjugated TSA® TSA-fluors (PerkinElmer; Opal 7-color IHC Kit, NEL797001KT, 1:100, 20–60 s), after which the primary and secondary antibodies were thoroughly eluted in glycine SDS pH 2 buffer for 40 min at 50°C. Nuclei were subsequently visualized with DAPI (1:2,000), and the slides were coverslipped using ProLong® Gold antifade mountant (ThermoFisher; P36934).

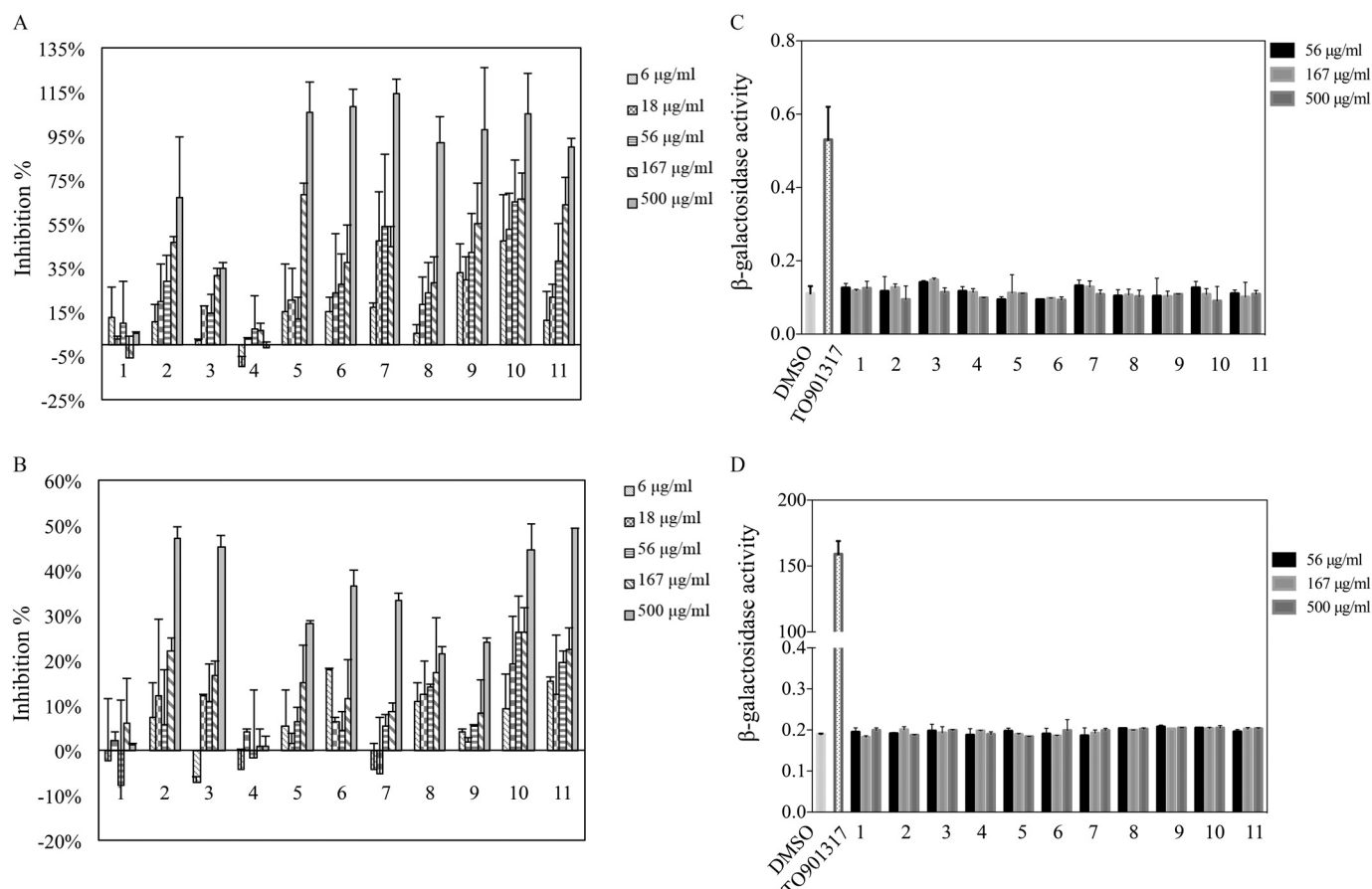


Figure 1. Yeast two-hybrid assay to evaluate LXR-agonistic and -antagonistic activity (means \pm SDs) of indoor dust samples. The (A) LXR α - and (B) LXR β -antagonistic activity of indoor dust samples (Samples 1–11). LXR-positive agonist, TO901317 (100 nM for LXR α and 220 nM for LXR β) along with indoor dust sample extracts were added to the medium. Inhibition percentage was estimated as the β -galactosidase inhibition compared with TO901317-treated group (100 nM for LXR α and 220 nM for LXR β) by Equation 2 in the main text. The (C) LXR α - and (D) LXR β -agonistic activity of indoor dust samples (Samples 1–11). One percent DMSO and TO901317 (100 nM for LXR α and 220 nM for LXR β) were used as the negative control and the positive control, respectively. $n = 3$. Note: LXR, liver X receptor; SD, standard deviation.

Statistical Analysis

One-way analysis of variance (ANOVA) followed by a post hoc Dunnett's test was performed using SPSS (version 16.0; SPSS Inc.) to determine the statistical significance of the results. Student's *t*-test was used to analyze the data of the pull-down assay combined with the chemical analysis. For the animal experiments, the Mann-Whitney *U*-test was applied. Results with $p < 0.05$ were considered to be statistically significant. The number of replicates is indicated in the figure legends. The nontarget chemical analysis, yeast two-hybrid assay, cell viability, qRT-PCR, cellular cholesterol efflux assay, and foam cell formation experiment were performed at least three times. For the experiments with the ApoE $^{-/-}$ mouse model, experiments were performed twice with $n = 4$ and 5.

Results

Identification of LXR Ligands in Indoor Dust

LXR-agonistic and -antagonistic activities of extracts of 11 indoor dust samples (Samples 1–11) were assessed using a yeast two-hybrid assay. TO901317, the LXR-agonist positive control, induced β -galactosidase activity in a dose-dependent manner in both LXR α and LXR β assays, and its EC₅₀ was 100 nM for LXR α and 220 nM for LXR β (see Figure S2). In a screening of

indoor dust samples, we unexpectedly discovered that 9 of the 11 indoor dust samples showed dose-dependent LXR-antagonist activity induced by TO901317 in LXR α and LXR β assays (Figure 1A,B). However, no indoor dust samples showed LXR-agonist activity (Figure 1C,D). Seven indoor dust samples (i.e., Samples 5–11) completely inhibited β -galactosidase activity in an LXR α assay at the concentration of 500 μ g indoor dust/mL. Four samples (i.e., Samples 2, 3, 10, and 11) inhibited approximately 50% of the β -galactosidase activity in an LXR β assay.

To identify chemicals with LXR-binding activity, we combined a His-LXR α pull-down assay with a nontarget HRMS method. Using freshly purified LXR α protein (see Figure S1), LXRs ligands were pulled down from the indoor dust extracts. The elution extracts from the control and the His-TF-LXR α group were analyzed to identify LXR α ligands in indoor dust samples using nontarget HRMS chemical analysis. PCA of the spectral data revealed that samples exhibiting similar variances were clustered together, with the control and His-TF-LXR α groups showing notable differences (see Figure S3). These results suggest that LXR α specifically pulled down LXR ligands from the extracts of indoor dust. The 195 peaks in the His-TF-LXR α group showed a 3-fold higher abundance than those in the control group ($p < 0.05$) (Figure 2A). Based on the mass error and isotopic difference, the molecular formulas of 147 peaks could be

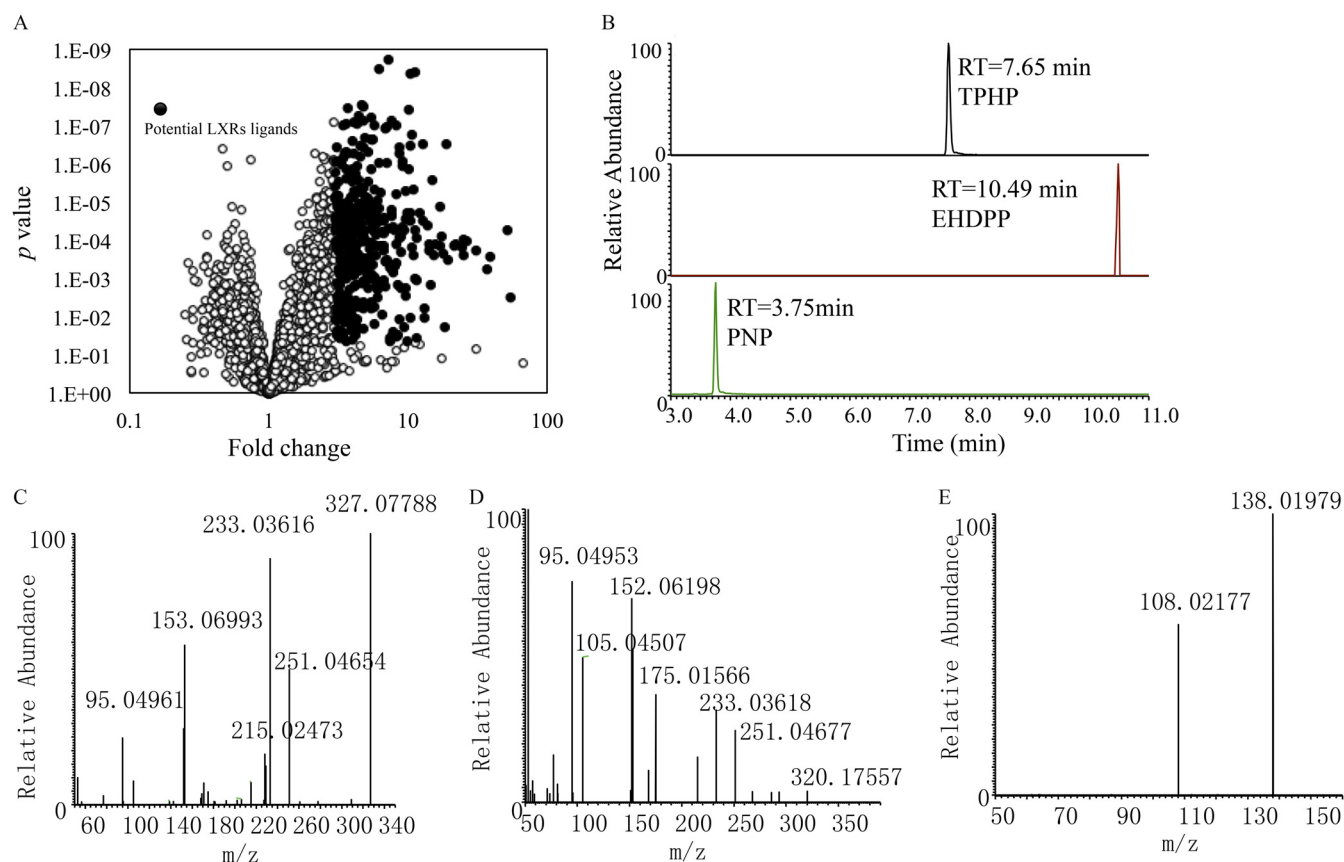


Figure 2. Identification of LXR ligands from indoor dust samples. Identification of differentiated peaks between the His-TF (control) and His-TF-LXR α group by nontarget chemical analysis using high-resolution mass spectrometry. (A) Only peaks exhibiting 3-fold higher abundance in His-TF-LXR α group than the control ($p < 0.05$; analyzed by Student's t -test) in volcano plot were considered to be potential ligands (closed circles) ($n = 6$). (B) Extracted chromatograms of triphenyl phosphate (TPHP), 2-ethylhexyl diphenyl phosphate (EHDPP), and p -nitrophenol (PNP) in the extract of indoor dust mixture sample of Samples 1–11. Mass spectra of (C) TPHP, (D) EHDPP, and (E) PNP in the extract of indoor dust mixture sample of Samples 1–11. Note: LXR, liver X receptor; TF, trigger factor.

calculated using Progenesis[®] QI software, and the formulas with the highest scores are shown in Excel Table S1. Of the obtained peaks, the mass spectra of three chromatographic peaks at retention times of 3.75, 7.65, and 10.49 min (Figure 2B), were well matched with the respective mass spectra of PNP and two organophosphate flame retardants (OPFRs)—TPHP, and EHDPP—in the mzCloud mass spectrum database (Figure 2C–E). TPHP, EHDPP, and PNP were further confirmed by comparing the retention times and MS/MS spectra to those of standards (see Figures S4 and S5).

LXR-Agonist and -Antagonist Activities of Identified Chemicals

The LXR-agonist and -antagonist activities of the three identified chemicals were evaluated using yeast two-hybrid assays. PNP showed weak LXR-agonist activity, with EC_{50} values of 14,020 nM for LXR α and 15,090 nM for LXR β . TPHP and EHDPP significantly inhibited β -galactosidase activity induced by 100 nM TO901317 in an LXR α yeast assay, with IC_{50} values of 1,477 nM [95% confidence interval (CI): 1,037, 2,103 nM] and 5,691 nM (95% CI: 3,658, 8,853 nM), respectively (Figure 3A). TPHP and EHDPP also significantly inhibited β -galactosidase activity induced by 220 nM TO901317 in an LXR β yeast assay, with IC_{50} values of 762 nM (95% CI: 229.9, 1,622 nM) and 2,165 nM (95% CI: 1,622, 4,233 nM), respectively (Figure 3B). TPHP was found to possess especially strong LXR α - and LXR β -antagonist activity, similar to SR9238, a positive antagonist of LXRs

(SR9238 IC_{50} : 824.7 nM for LXR α and 446.4 nM for LXR β) (Figure 3A,B).

LXR-antagonist activities were also observed in the indoor dust samples from Shanghai, Guangzhou, and Chongqing. Of the 18 indoor dust samples, 12 samples also showed dose-dependent

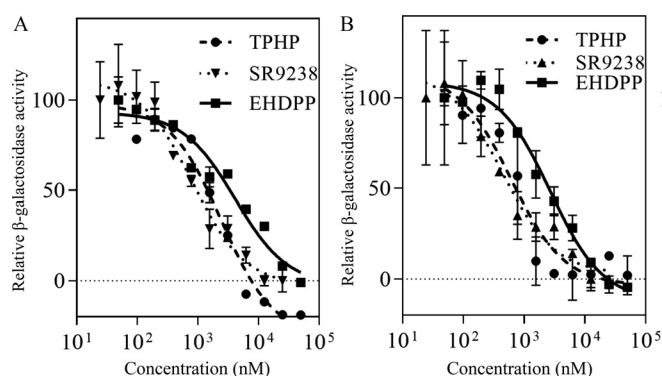


Figure 3. Yeast two-hybrid assay to evaluate LXR-antagonistic activity (means \pm SDs) of TPHP and EHDPP. The (A) LXR α - and (B) LXR β -antagonistic activity of TPHP and EHDPP in comparison with that of the positive LXR antagonist, SR9238. The LXR-positive agonist TO901317 (100 nM for LXR α and 220 nM for LXR β) along with TPHP, EHDPP, or SR9238 were added to the medium. $n = 3$. Note: EHDPP, 2-ethylhexyl diphenyl phosphate; LXR, liver X receptor; SD, standard deviation; TPHP, triphenyl phosphate.

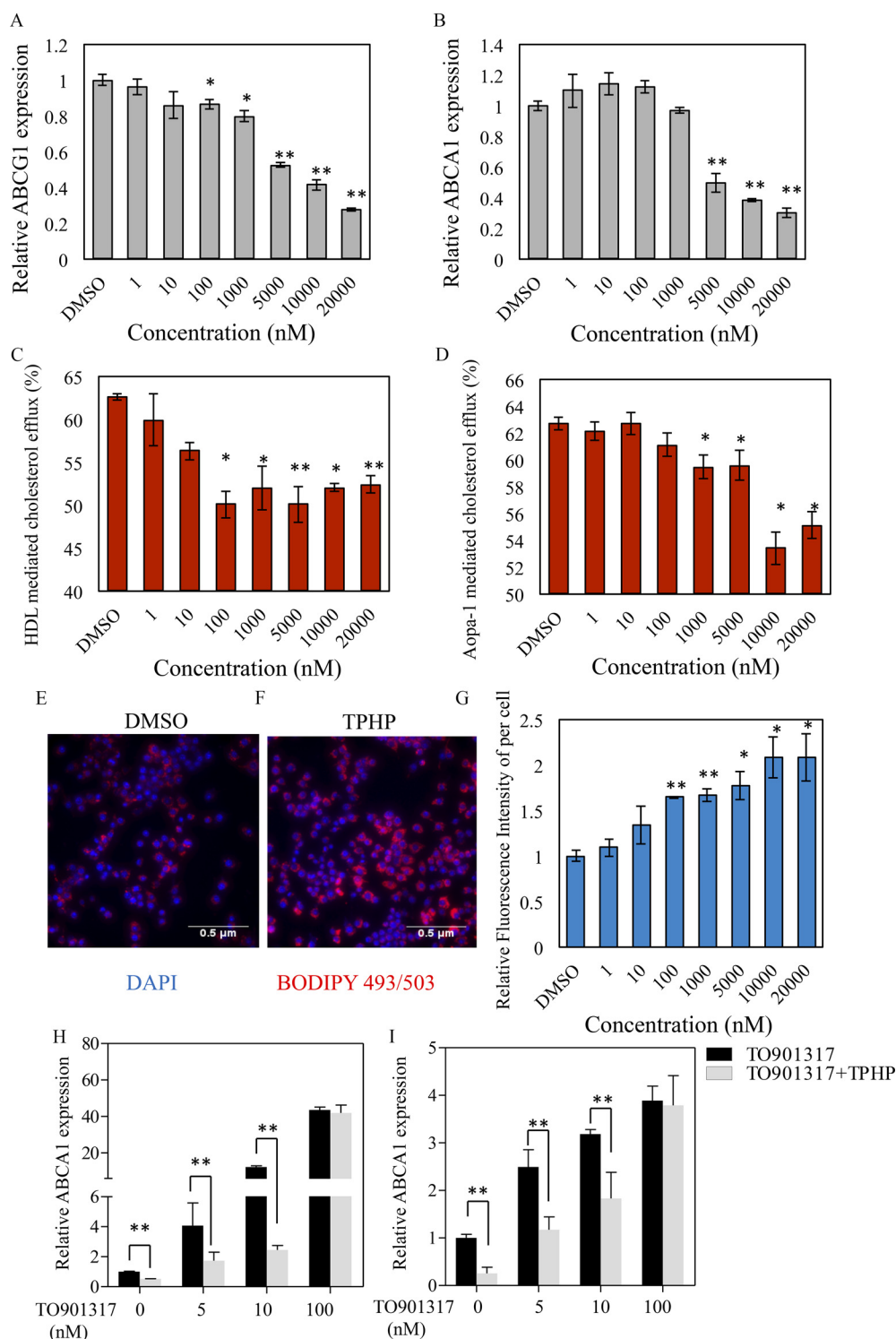


Figure 4. Gene expression (means \pm SDs) of LXR target genes, cholesterol efflux, and foam cell formation in RAW264.7 cells treated with TPHP. Quantitative analysis of (A) *ABCA1* and (B) *ABCG1* gene expression in RAW264.7 macrophages treated with TPHP. Data are expressed relative to the levels of vehicle-treated cells, which were set to 1. Cholesterol efflux in the presence of (C) HDL or (D) ApoA-I from RAW264.7 macrophages loaded with NBD-cholesterol and treated with DMSO or TPHP at concentration ranges from 1 nM to 20,000 nM and no significant loss of cell viability was observed (see Figure S7). Relative NBD-cholesterol efflux to HDL or ApoA-I induced by TPHP was calculated. (E) BODIPY 493/503 staining of RAW264.7 macrophages treated with ox-LDL, and exposed with (E) DMSO or (F) TPHP at 1–20,000 nM. (G) Quantitative analysis of foam cell formation in RAW264.7 macrophages treated with TPHP. Quantitative analysis of (H) *ABCA1* and (I) *ABCG1* gene expression in RAW264.7 macrophages treated with TPHP (10,000 nM) and co-exposed to TO901317 at 5–100 nM. Data are expressed relative to the levels of vehicle-treated cells, which were set to 1. $n = 3$. Analyzed by one-way ANOVA. Indicated values are significantly different from vehicle/control value. Note: ANOVA, analysis of variance; BODIPY, boron-dipyrromethene; DMSO, dimethyl sulfoxide; EHDPP, 2-ethylhexyl diphenyl phosphate; HDL, high-density-lipoprotein; LXR, liver X receptor; NBD, 22-[N-(7-nitrobenz-2-oxa-1,3-diazol-4-yl)amino]-23,24-bisnor-5-cholesterol-3 β -ol; ox-LDL, oxidized low-density-lipoprotein; SD, standard deviation; TPHP, triphenyl phosphite. * $p < 0.05$. ** $p < 0.01$.

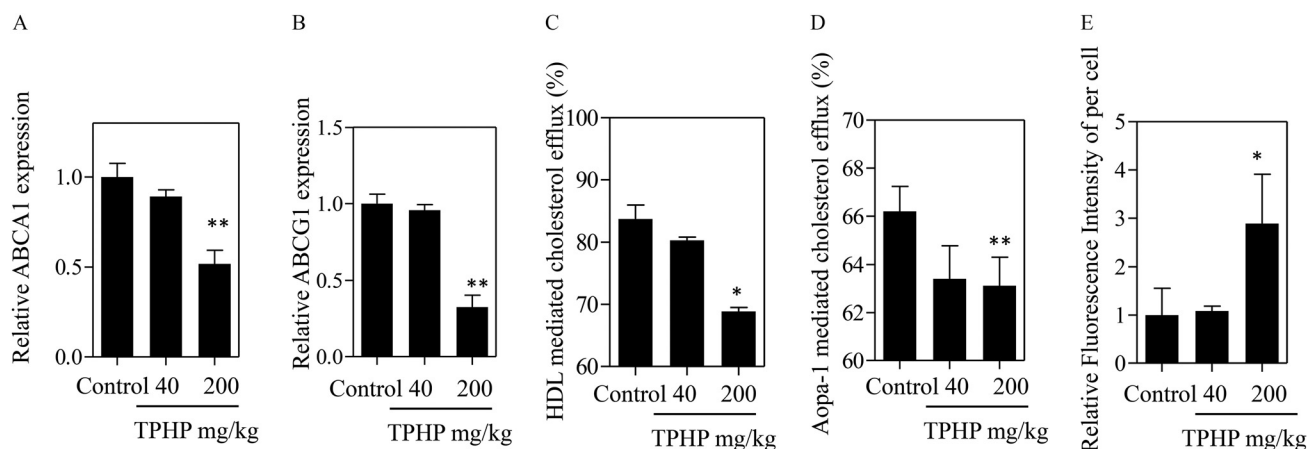


Figure 5. Gene expression (means \pm SDs) of LXR target genes, cholesterol efflux, and foam cell formation in peritoneal macrophages from animals treated with vehicle or TPHP for 7 d. C57BL/6 mice were exposed to TPHP at 40 and 200 mg/kg BW for 7 d, and the peritoneal macrophages were isolated. Quantitative analysis of (A) *ABCA1* and (B) *ABCG1* gene expressions in peritoneal macrophages. Data are expressed relative to the levels of vehicle/control group, which was set to 1. Cholesterol efflux in the presence of (C) HDL or (D) ApoA-I from peritoneal macrophages loaded with NBD-cholesterol. Relative NBD-cholesterol efflux to HDL or ApoA-I induced by TPHP was calculated. (E) Foam cell formation of peritoneal macrophages treated with ox-LDL. $n=5$. Analyzed by one-way ANOVA. Indicated values are significantly different from vehicle/control value. Note: ANOVA, analysis of variance; BW, body weight; EHDPP, 2-ethylhexyl diphenyl phosphate; HDL, high-density-lipoprotein; LXR, liver X receptor; NBD, 22-[N-(7-nitrobenz-2-oxa-1,3-diazol-4-yl)amino]-23,24-bisnor-5-cholen-3 β -ol; ox-LDL, oxidized low-density-lipoprotein; TPHP, triphenyl phosphite. * $p < 0.05$. ** $p < 0.01$.

LXR-antagonist activity induced by TO901317 in LXR α and LXR β assays (see Figure S6). The TPHP and EHDPP concentrations in the indoor dust extracts tested in the present study were determined to estimate their contribution to total LXR-antagonist activity. TPHP and EHDPP concentrations were 0.13–12.28 $\mu\text{g/g}$ and 0.01–0.61 $\mu\text{g/g}$, respectively (see Table S4). TPHP explained 0.19–51.07% of the LXR α -antagonist activity and 0.37–32.60% of the LXR β -antagonist activity of indoor dust; 0.01–25.02% of the LXR α -antagonist activity and 0.01–22.92% of the LXR β -antagonist activity of indoor dust were contributed by EHDPP (see Table S4). The dust standard reference material SRM2585 also exhibited LXR-antagonist activity, and the inhibition could be observed at 167 μg indoor dust/mL, and 28.4% and 46.8% of the β -galactosidase activity of LXR α and LXR β were inhibited at 500 μg indoor dust/mL. TPHP and EHDPP contributed 33.83% and 3.01% of the LXR α -antagonist activity, and 12.68% and 1.55% of the LXR β -antagonist activity of SRM2585.

Treatment of Macrophages with TPHP and Evaluation of Foam Cell Formation

Because TPHP exhibited the strongest LXR-antagonist activity, we tested the variation in the mRNA levels of two representative direct LXR target genes, *ABCA1* and *ABCG1* (Smith et al. 1995; Wang et al. 2007), in RAW264.7 macrophages exposed to TPHP. Confluent RAW264.7 macrophages showed no significant loss of cell viability after 24-h exposure to TPHP at 1–20,000 nM concentrations (see Figure S7). The *ABCG1* gene expression was significantly down-regulated by 0.87 ± 0.05 -, 0.80 ± 0.06 -, 0.52 ± 0.02 -, 0.42 ± 0.05 -, and 0.28 ± 0.02 -fold in the 100 ($p < 0.05$), 1,000 ($p < 0.05$), 5,000 ($p < 0.01$), 10,000 ($p < 0.01$), and 20,000 nM ($p < 0.01$) TPHP-exposure groups, respectively, relative to the control group, indicating a dose–response relationship. Significant down-regulation of *ABCA1* was also observed in 5,000, 10,000, and 20,000 nM TPHP-exposure groups by 0.49 ± 0.06 -, 0.38 ± 0.01 -, and 0.30 ± 0.03 -fold, respectively, relative to the control group ($p < 0.01$) (Figure 4A,B).

We further assessed the effects of TPHP on NBD-cholesterol efflux from RAW264.7 macrophages and found that the cholesterol efflux mediated by ApoA-I and HDL was significantly inhibited by 100–20,000 nM and 1,000–20,000 nM TPHP, respectively

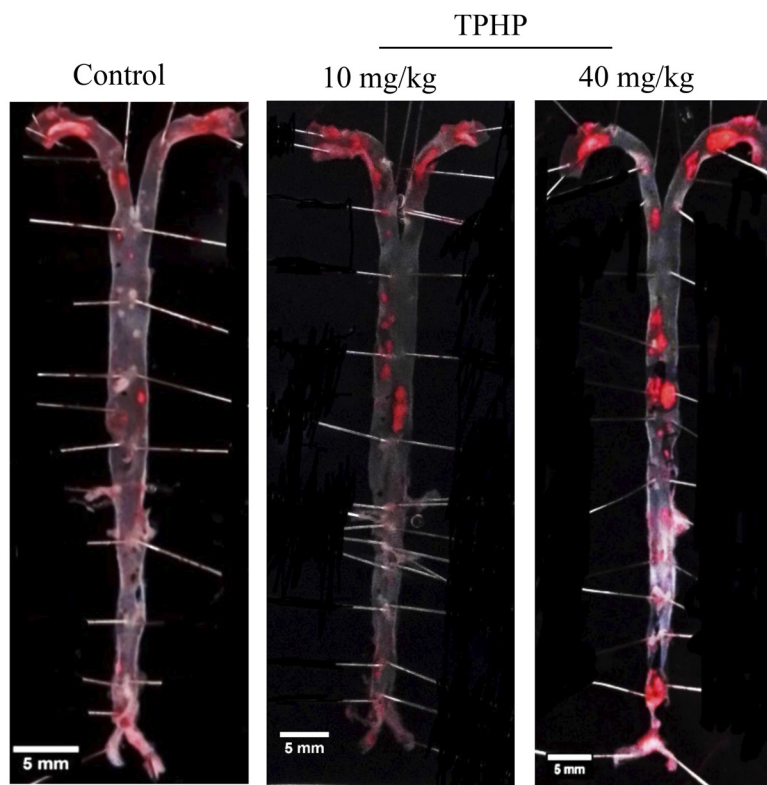
(Figure 4C,D). The effects of TPHP on foam cell formation were further investigated in RAW264.7 macrophages. The intensity of foam cell staining in RAW264.7 macrophages was significantly greater by 1.64 ± 0.02 -, 1.67 ± 0.14 -, 1.78 ± 0.31 -, 2.08 ± 0.45 -, and 2.09 ± 0.52 -fold in the 100 ($p < 0.01$), 1,000 ($p < 0.01$), 5,000 ($p < 0.05$), 10,000 ($p < 0.05$), and 20,000 nM ($p < 0.05$) TPHP-exposure groups, respectively, relative to that in the control group (Figure 4E–G). *ABCA1* and *ABCG1* gene expression in RAW264.7 macrophages exposed to TPHP at 10,000 nM was dose-dependently higher in TO901317-treated cells than in cells treated with TPHP alone (Figure 4H,I).

ABCA1 and *ABCG1* gene expression in peritoneal macrophages isolated from mice exposed to TPHP at 200 mg/kg BW for 7 d was also significantly down-regulated by 0.51 ± 0.07 - and 0.30 ± 0.08 -fold, respectively, compared with the control ($p < 0.01$) (Figure 5A,B). Significant inhibition of ApoA-I- and HDL-mediated cholesterol efflux was observed in 200 mg/kg BW TPHP exposure (Figure 5C,D), and foam cell staining was higher by 2.88 ± 0.95 -fold compared with that in the control ($p < 0.05$) (Figure 5E).

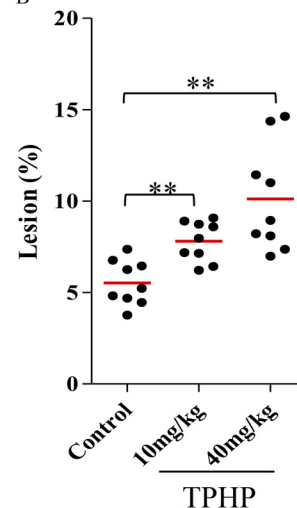
Atherosclerotic Lesion Formation in the ApoE $^{-/-}$ Mouse Model

Foam cells play a central role in atherosclerosis development (Tontonoz and Mangelsdorf 2003). To demonstrate whether TPHP could exacerbate atherosclerosis, we exposed ApoE $^{-/-}$ mice to TPHP at 10 and 40 mg/kg BW for 13 weeks. No significant differences in BW were observed (see Figure S8). However, *en face* analysis of the whole atherosclerotic lesion and the entire aorta showed a stark contrast between the control and TPHP-exposure groups (Figure 6A). *En face* lipid staining showed the area of the atherosclerotic lesion in the 10 and 40 mg/kg BW TPHP-exposure groups were 41% and 83% higher than that of the control group ($p < 0.01$), respectively (Figure 6B). Because atherosclerotic lesions generally develop first in the aortic root, we also analyzed lesion areas in the aortic root. Quantification of the area covered by the atherosclerotic lesion around the aortic root revealed a significantly higher lesion area in the TPHP-exposure groups than that of the control ($p < 0.01$) (Figure 6C,D). In order to further characterize the atherosclerotic lesions, we

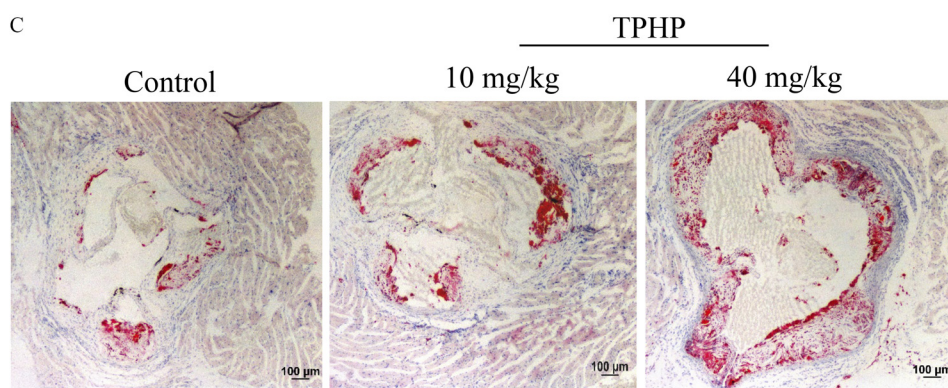
A



B



C



D

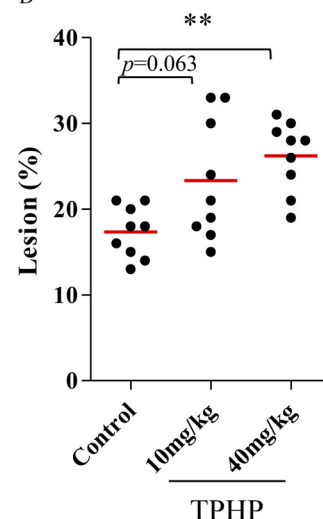


Figure 6. Atherosclerotic plaque formation in ApoE^{-/-} mice treated with vehicle or TPHP for 13 weeks. (A) Representative *en face* Oil red O staining of aortas of mice exposed to TPHP compared with the control group. (B) The plaque area is presented as lesion percentage (of whole aorta) in the graph ($n=9$). (C) Representative Oil red O staining of the aortic root sections. (D) The graph represents the quantification of the area positive for lipid staining $n=9$). Analyzed by Mann-Whitney U -test. Indicated values are significantly different from vehicle/control value. Note: TPHP, triphenyl phosphite. * $p < 0.05$. ** $p < 0.01$.

used immunofluorescence staining of the aortic root sections to determine the contents of MOMA-2-positive macrophages and SMC α -Actin-positive smooth muscle cells (SMCs) in the atherosclerotic lesions (Figure 7A). A significantly higher macrophage abundance was observed in the aortic roots of TPHP-exposed mice. Specifically, the macrophage content was 1.9- and 3.1-fold higher in the 10 ($p < 0.05$) and 40 mg/kg ($p < 0.01$) BW TPHP-exposure groups than in the control group (Figure 7B). However, for the abundance of SMCs in the aortic roots, a significant difference was not found between the TPHP-exposed groups and the control (Figure 7C). Further analyses found that the serum TC and TG levels were significantly higher in the 40 mg/kg BW TPHP-exposure group than in the control group (Table 1). However, we also found that LDL-C and HDL-C levels of the two exposure groups were not significantly different from those in the control group.

Discussion

To date, few toxicological studies have investigated the LXR-antagonist activity of environmental samples. This study revealed that among 29 indoor house dust samples from nine cities in China, 21 exhibited dose-dependent LXR-antagonist activity, suggesting that LXR-antagonist activity in indoor dust may be relatively common. Because environmental samples such as indoor dust are chemically complex and contain a multitude of organic contaminants, the identification of specific chemicals in indoor dust that possess LXR-antagonist activity is challenging. We used an LXR α pull-down assay combined with a nontarget HRMS method to isolate and identify those chemicals that could interact with LXR α from indoor dust. In this study, 147 chemicals with LXR α -binding activity were found in indoor dust. Although many putative LXR ligands could not be identified

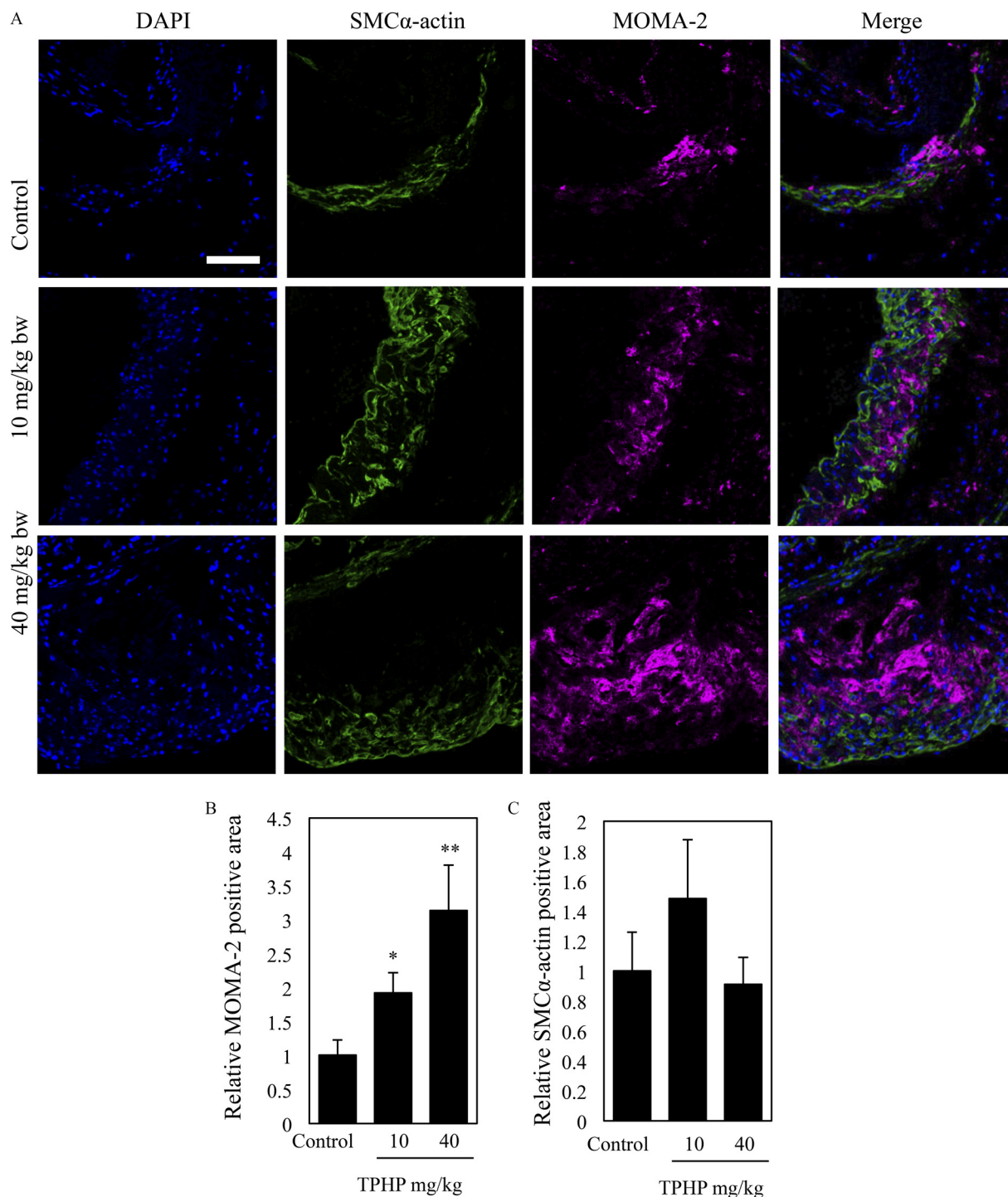


Figure 7. Characterization of macrophage and smooth muscle cell content (means \pm SDs) of atherosclerosis lesion in ApoE^{-/-} mice treated with vehicle or TPHP for 13 weeks. (A) Representative histology of the aortic root sections stained with DAPI, smooth muscle cells marker (SMC α -Actin), and macrophage marker (MOMA-2). The graphs represent the quantification of the relative positive area of cellular elements (B) MOMA-2 and (C) SMC α -Actin. Bar: 100 μ m. $n=9$). Analyzed by Mann-Whitney U -test. Indicated values are significantly different from vehicle/control value. Note: DAPI, 4',6-diamidino-2-phenylindole; SD, standard deviation; TPHP, triphenyl phosphite. * $p < 0.05$. ** $p < 0.01$.

because the recorded spectra of standards in available mass spectra database are still limited, two OPFRs, namely TPHP and EHDPP, were identified as LXR antagonists in house dust samples from Chinese cities. TPHP exhibited strong LXR α - and LXR β -antagonistic activity, similar to that of SR9238, a positive antagonist of LXRs (Figure 3A,B). TPHP and EHDPP are widely used as flame retardants and plasticizers in various consumer products (including soft foams, paints, and wallpaper) and

building materials (Wei et al. 2015). TPHP and EHDPP have been detected in indoor dust, and TPHP is one of the most predominant pollutants in the indoor dust samples collected between January and March 2002 in Tokyo, where it was found at concentrations as high as 20,700 μ g/g (Saito et al. 2007). In our study, TPHP was found to explain 0.19–51.07% of the LXR α -antagonist activity and 0.37–32.60% of the LXR β -antagonist activity of indoor dust (see Table S4). EHDPP explained 0.01–25.02%

Table 1. Plasma lipid levels [mean \pm SE (mmol/L)] in ApoE^{-/-} mice after 13-week treatment of TPHP.

	Cholesterol	Triglycerides	HDL-C	LDL-C
Control	23.19 \pm 1.21	0.77 \pm 0.06	1.22 \pm 0.04	10.16 \pm 0.36
10 mg/kg	26.15 \pm 1.34	0.92 \pm 0.06	1.13 \pm 0.05	10.53 \pm 0.32
40 mg/kg	28.83 \pm 1.90*	1.06 \pm 0.12*	1.29 \pm 0.05	10.27 \pm 0.22

Note: $n = 9$ per group. HDL-C, high-density lipoprotein cholesterol; LDL-C, low-density lipoprotein cholesterol; SE, standard error; TPHP, triphenyl phosphate. * $p < 0.05$ (analyzed by Mann-Whitney U -test) indicate values significantly different from vehicle/control value.

of the LXR α -antagonist activity and 0.01–22.92% of the LXR β -antagonist activity of indoor dust (see Table S4). Thus, other contaminants contributed a large part of the LXR-antagonist activity of indoor dust, and further identification is needed.

Although the synthetic LXR agonist GW3965 has been reported to inhibit foam cell formation in both macrophages and in the atherosclerosis mouse model (Joseph et al. 2002) and chemicals that can activate LXRs are designed to treat atherosclerosis, the LXR activity of organic pollutants and associated atherosclerosis risk have not yet been assessed. This study revealed that TPHP promoted foam cell formation in RAW264.7 macrophages (Figure 4E) and in mice peritoneal macrophages. Foam cell formation may be attributable to TPHP-inhibited cholesterol efflux (Figure 4C,D) given that attenuating excess cellular cholesterol efflux has previously been reported to be the causal factor for foam cell formation (Cuchel and Rader 2006). *ABCA1* and *ABCG1* gene expressions in macrophages play a critical role in the efflux of excess cellular cholesterol to Apo acceptors such as ApoA-I and HDL (Smith et al. 1995; Wang et al. 2007), and the selective inactivation of *ABCA1* and *ABCG1* in macrophages causes an imbalance between uptake and *ABCA1* and *ABCG1*-mediated cholesterol efflux (Hagpassand et al. 2001; Van Eck et al. 2002; N Wang et al. 2000, 2004). In the present study, TPHP down-regulated *ABCA1* and *ABCG1* expression in macrophages in a dose-response manner (Figure 4A,B), demonstrating that the TPHP-induced foam cell formation might be mediated by LXRs given that *ABCA1* and *ABCG1* are downstream target genes of LXRs in macrophages (Smith et al. 1995; Wang et al. 2007).

In this study, a well-established atherosclerosis model, the ApoE^{-/-} mouse, was used to evaluate the atherosclerotic activity of TPHP *in vivo*. The development from initial fatty streaks to complex lesions observed in ApoE^{-/-} mice resembles that in human, whereas wild-type mice are highly resistant to atherosclerosis (Breslow 1996). In ApoE^{-/-} mice exposed to 10 and 40 mg/kg BW of TPHP, *en face* lipid staining revealed significant promotion of the atherosclerotic lesion and plaque area in the aortic roots (Figure 6). TPHP exposure at 40 mg/kg BW significantly promoted plasma TC and TG levels (Table 1). Although the alterations in plasma lipid profiles might have contributed to atherosclerosis development in mouse, it may be insufficient to explain the promotion in atherosclerotic lesions because substantial changes in TC and TG levels occurred only in the 40 mg/kg BW TPHP-exposure group. It has been reported that TPHP is the agonist of peroxisome proliferator-activated receptor- γ (PPAR γ) (Hu et al. 2017; Pillai et al. 2014). PPAR γ plays an essential role in regulating adipogenesis (Tontonoz and Spiegelman 2008), and TPHP has been shown to promote adipogenesis in human primary preadipocytes (Tung et al. 2017). In addition to adipogenesis, obesity has been also observed after *in utero* and lactational exposure to TPHP and was reported to result from modulation of the gut microbiome composition of mice (Wang et al. 2019). In this study, no significant BW change was observed in ApoE^{-/-} mice (fed a high-fat diet) after 13-week exposure to TPHP, compared with the control. This may be due to the fact that the absence of ApoE would reduce the BW and induce some of the obesity-associated metabolic complications,

including impaired glucose tolerance and insulin resistance in obese models, given that ApoE has been shown to play a key role in energy metabolism in adipose tissue (Chiba et al. 2003; Gao et al. 2007; Karagiannides et al. 2008; Pendse et al. 2009).

Our results demonstrate that TPHP exposure promoted foam cell formation in RAW264.7 macrophages and in peritoneal macrophages isolated from TPHP treatment mice (Figures 4E and 5E). The foam cells facilitate adventitia angiogenesis and the buildup of necrotic pools, thereby leading to atherosclerosis exacerbation and plaque instability (Bensinger et al. 2008). The importance of foam cells in atherosclerosis has been demonstrated by the lack of atherosclerotic lesions in the macrophage-deficient mouse (Smith et al. 1995). Foam cells play a central role in atherosclerosis development and are prominent cellular elements in atherosclerotic plaque pathogenesis (Tontonoz and Mangelsdorf 2003). Analysis of the atherosclerosis lesion composition also revealed a significantly higher macrophage content in the aortic valves of mice exposed to 10 and 40 mg/kg BW TPHP in the ApoE^{-/-} mouse model (Figure 7). These results collectively suggest that the TPHP-promoted atherosclerosis in the ApoE^{-/-} mouse model is largely attributable to foam cell formation within the artery wall mediated by LXR pathways.

This work assessed the LXR-antagonist activity of TPHP *in vitro* and *in vivo* in an atherosclerosis mouse model and demonstrated that TPHP may pose an atherosclerosis risk in the mouse. Moreover, TPHP contributed only a part of the LXR-antagonist activity of indoor dust (see Table S4), leading us to suspect that indoor dust contains other chemicals with LXR-antagonist activity and that these chemicals also may heighten atherosclerosis risk. Ultimately, observations of atherosclerosis induced by chemical pollutants via LXR-signaling pathways in the present paper promote the understanding of the environmental chemicals that might also affect cardiovascular health in humans and illustrate that a comprehensive assessment of the LXR-inactivating potential should be an important part of chemical management to ensure the protection of human health.

Acknowledgments

We thank X. Li and G. Li from Core Facilities, School of Life Sciences, Peking University for assistance with the ImageXpress[®] Micro XL and AKTA pure protein purification system. This study received financial support from the International S&T Cooperation Program of China (2016YFE0117800) and the National Natural Science Foundation of China (21737001, 21577001, and 41821005).

References

- Bensinger SJ, Bradley MN, Joseph SB, Zelcer N, Janssen EM, Hausner MA, et al. 2008. LXR signaling couples sterol metabolism to proliferation in the acquired immune response. *Cell* 134(1):97–111, PMID: 18614014, <https://doi.org/10.1016/j.cell.2008.04.052>.
- Bergman Å, Heindel JJ, Jobling S, Kidd KA, Zoeller RT. 2013. *The State-of-the-Science of Endocrine Disrupting Chemicals*. Geneva, Switzerland: United Nations Environment Programme, World Health Organization.
- Bhatnagar A. 2004. Cardiovascular pathophysiology of environmental pollutants. *Am J Physiol Heart Circ Physiol* 286(2):H479–H485, PMID: 14715496, <https://doi.org/10.1152/ajpheart.00817.2003>.
- Bhatnagar A. 2006. Environmental cardiology: studying mechanistic links between pollution and heart disease. *Circ Res* 99(7):692–705, PMID: 17008598, <https://doi.org/10.1161/01.RES.0000243586.99701.cf>.
- Breslow JL. 1996. Mouse models of atherosclerosis. *Science* 272(5262):685–688, PMID: 8614828, <https://doi.org/10.1126/science.272.5262.685>.
- Brook RD, Franklin B, Cascio W, Hong Y, Howard G, Lipsett M, et al. 2004. Air pollution and cardiovascular disease: a statement for healthcare professionals from the Expert Panel on Population and Prevention Science of the American Heart Association. *Circulation* 109(21):2655–2671, PMID: 15173049, <https://doi.org/10.1161/01.CIR.0000128587.30041.C8>.
- Chen G, Jin Y, Wu Y, Liu L, Fu Z. 2015. Exposure of male mice to two kinds of organophosphate flame retardants (OPFRs) induced oxidative stress and endocrine disruption. *Environ Toxicol Pharmacol* 40 (1):310–318, PMID: 26183808, <https://doi.org/10.1016/j.etap.2015.06.021>.

- Chen WW, Gao RL, Liu LS, Zhu ML, Wang W, Wang YJ, et al. 2017. China cardiovascular diseases report 2015: a summary. *J Geriatr Cardiol* 14(1):1–10. PMC, PMID: 28270835, <https://doi.org/10.11909/j.issn.1671-5411.2017.01.012>.
- Chiba T, Nakazawa T, Yui K, Kaneko E, Shimokado K. 2003. VLDL induces adipocyte differentiation in ApoE-dependent manner. *Arterioscler Thromb Vasc Biol* 23(8):1423–1429, PMID: 12842848, <https://doi.org/10.1161/01.ATV.0000085040.58340.36>.
- Cuchel M, Rader DJ. 2006. Macrophage reverse cholesterol transport key to the regression of atherosclerosis? *Circulation* 113(21):2548–2555, PMID: 16735689, <https://doi.org/10.1161/CIRCULATIONAHA.104.475715>.
- Fang M, Webster TF, Ferguson PL, Stapleton HM. 2015. Characterizing the peroxisome proliferator-activated receptor (PPAR γ) ligand binding potential of several major flame retardants, their metabolites, and chemical mixtures in house dust. *Environ Health Perspect* 123(2):166–172, PMID: 25314719, <https://doi.org/10.1289/ehp.1408522>.
- Gao J, Katagiri H, Ishigaki Y, Yamada T, Ogihara T, Imai J, et al. 2007. Involvement of apolipoprotein E in excess fat accumulation and insulin resistance. *Diabetes* 56(1):24–33, PMID: 17192461, <https://doi.org/10.2337/db06-0144>.
- Glass CK, Witztum JL. 2001. Atherosclerosis: the road ahead. *Cell* 104(4):503–516, PMID: 11239408, [https://doi.org/10.1016/S0092-8674\(01\)00238-0](https://doi.org/10.1016/S0092-8674(01)00238-0).
- Haghighpassand M, Bourassa PAK, Francone DL, Aiello RJ. 2001. Monocyte/macrophage expression of ABCA1 has minimal contribution to plasma HDL levels. *J Clin Invest* 108(9):1315–1320, PMID: 11696576, <https://doi.org/10.1172/JCI200112810>.
- Hu W, Gao F, Zhang H, Hiromori Y, Arakawa S, Nagase H, et al. 2017. Activation of peroxisome proliferator-activated receptor gamma and disruption of progesterone synthesis of 2-ethylhexyl diphenyl phosphate in human placental chorioncarcinoma cells: comparison with triphenyl phosphate. *Environ Sci Technol* 51(7):4061–4068, PMID: 28282128, <https://doi.org/10.1021/acs.est.7b00872>.
- Joseph SB, McKilligin E, Pei L, Watson MA, Collins AR, Laffitte BA, et al. 2002. Synthetic LXR ligand inhibits the development of atherosclerosis in mice. *Proc Natl Acad Sci USA* 99(11):7604–7609, PMID: 12032330, <https://doi.org/10.1073/pnas.112059299>.
- Karagiannides I, Abdou R, Tzortzopoulou A, Voshol PJ, Kypreos KE. 2008. Apolipoprotein E predisposes to obesity and related metabolic dysfunctions in mice. *FEBS J* 275(19):4796–4809, PMID: 18754772, <https://doi.org/10.1111/j.1742-4658.2008.06619.x>.
- Kassotis CD, Hoffman K, Stapleton HM. 2017. Characterization of adipogenic activity of house dust extracts and semi-volatile indoor contaminants in 3T3-L1 cells. *Environ Sci Technol* 51(15):8735–8745, PMID: 28699343, <https://doi.org/10.1021/acs.est.7b01788>.
- Li K, Yao W, Zheng X, Liao K. 2009. Berberine promotes the development of atherosclerosis and foam cell formation by inducing scavenger receptor A expression in macrophage. *Cell Res* 19(8):1006–1017, PMID: 19546885, <https://doi.org/10.1038/cr.2009.76>.
- Meeker JD, Stapleton HM. 2010. House dust concentrations of organophosphate flame retardants in relation to hormone levels and semen quality parameters. *Environ Health Perspect* 118(3):318–323, PMID: 20194068, <https://doi.org/10.1289/ehp.0901332>.
- Morris PJ, Medina-Cleghorn D, Heslin A, King SM, Orr J, Mulvihill MM, et al. 2014. Organophosphorus flame retardants inhibit specific liver carboxylesterases and cause serum hypertriglyceridemia. *ACS Chem Biol* 9(5):1097–1103, PMID: 24597639, <https://doi.org/10.1021/cb500014r>.
- Negro Silva LF, Lemaire M, Lemarié CA, Plourde D, Bolt AM, Chiavatti C, et al. 2017. Effects of inorganic arsenic, methylated arsenicals, and arsenobetaine on atherosclerosis in the apo E^{−/−} mouse model and the role of As3mt-mediated methylation. *Environ Health Perspect* 125(7):077001, PMID: 28728140, <https://doi.org/10.1289/EHP806>.
- Pendse AA, Arbones-Mainar JM, Johnson LA, Altenburg MK, Maeda N. 2009. Apolipoprotein E knock-out and knock-in mice: atherosclerosis, metabolic syndrome, and beyond. *J Lipid Res* 50(Suppl):S178–S182, PMID: 19060252, <https://doi.org/10.1194/jlr.R800070-JLR200>.
- Pennings M, Meurs I, Ye D, Out R, Hoekstra M, Van Berkel TJC, et al. 2006. Regulation of cholesterol homeostasis in macrophages and consequences for atherosclerotic lesion development. *FEBS Lett* 580(23):5588–5596, PMID: 16935283, <https://doi.org/10.1016/j.febslet.2006.08.022>.
- Pillai HK, Fang M, Beglov D, Kozakov D, Vajda S, Stapleton HM, et al. 2014. Ligand binding and activation of PPAR γ by Firemaster[®] 550: effects on adipogenesis and osteogenesis *in vitro*. *Environ Health Perspect* 122(11):1225–1232, PMID: 25062436, <https://doi.org/10.1289/ehp.1408111>.
- Roger VL, Go AL, Lloyd-Jones DM, Benjamin EJ, Berry JD, Borden WB, et al. 2012. Heart disease and stroke statistics—2012 update: a report from the American Heart Association. *Circulation* 125(1):e2–e220, PMID: 22179539, <https://doi.org/10.1161/CIR.0b013e31823ac046>.
- Saeed O, Otsuka F, Polavarapu R, Karmali V, Weiss D, Davis T, et al. 2012. Pharmacological suppression of hepcidin increases macrophage cholesterol efflux and reduces foam cell formation and atherosclerosis. *Arterioscler Thromb Vasc Biol* 32(2):299–307, PMID: 22095982, <https://doi.org/10.1161/ATVBAHA.111.240101>.
- Saito I, Onuki H, Seto H. 2007. Indoor organophosphate and polybrominated flame retardants in Tokyo. *Indoor Air* 17(1):28–36, PMID: 17257150, <https://doi.org/10.1111/j.1600-0668.2006.00442.x>.
- Shi H, Mao X, Zhong Y, Liu Y, Zhao X, Yu K, et al. 2016. Lanatoside C promotes foam cell formation and atherosclerosis. *Sci Rep* 6:20154, PMID: 26821916, <https://doi.org/10.1038/srep20154>.
- Smith JD, Trogan E, Ginsberg M, Grigaux C, Tian J, Miyata M. 1995. Decreased atherosclerosis in mice deficient in both macrophage colony-stimulating factor (op) and apolipoprotein E. *Proc Natl Acad Sci USA* 92(18):8264–8268, PMID: 7667279, <https://doi.org/10.1073/pnas.92.18.8264>.
- Schneider CA, Rasband WS, Eliceiri KW. 2012. NIH Image to ImageJ: 25 years of image analysis. *Nat Methods* 9:671–675, PMID: 22930834, <https://doi.org/10.1038/nmeth.2089>.
- Suzuki G, Tue NM, Malarvannan G, Sudaryanto A, Takahashi S, Tanabe S, et al. 2013. Similarities in the endocrine-disrupting potencies of indoor dust and flame retardants by using human osteosarcoma (U2OS) cell-based reporter gene assays. *Environ Sci Technol* 47(6):2898–2908, PMID: 23398518, <https://doi.org/10.1021/es304691a>.
- Tangirala RK, Bischoff ED, Joseph SB, Wagner BL, Walczak R, Laffitte BA, et al. 2002. Identification of macrophage liver X receptors as inhibitors of atherosclerosis. *Proc Natl Acad Sci USA* 99(18):11896–11901, PMID: 12193651, <https://doi.org/10.1073/pnas.182199799>.
- Terasaka N, Hiroshima A, Koieyama T, Ubukata N, Morikawa Y, Nakai D, et al. 2003. T-0901317, a synthetic liver X receptor ligand, inhibits development of atherosclerosis in LDL receptor-deficient mice. *FEBS Lett* 536(1–3):6–11, PMID: 12586329, [https://doi.org/10.1016/S0014-5793\(02\)03578-0](https://doi.org/10.1016/S0014-5793(02)03578-0).
- Tontonoz P, Mangelsdorf DJ. 2003. Liver X receptor signaling pathways in cardiovascular disease. *Mol Endocrinol* 17(6):985–993, PMID: 12690094, <https://doi.org/10.1210/me.2003-0061>.
- Tontonoz P, Spiegelman BM. 2008. Fat and beyond: the diverse biology of PPAR γ . *Annu Rev Biochem* 77:289–312, PMID: 18518822, <https://doi.org/10.1146/annurev.biochem.77.061307.091829>.
- Tung EWY, Peshdary V, Gagné R, Rowan-Carroll A, Yauk CL, Boudreau A, et al. 2017. Adipogenic effects and gene expression profiling of Firemaster[®] 550 components in human primary preadipocytes. *Environ Health Perspect* 125(9):097013, PMID: 28934090, <https://doi.org/10.1289/EHP1318>.
- Van Eck M, Bos IS, Kaminski WE, Orsó E, Rothe G, Twisk J, et al. 2002. Leukocyte ABCA1 controls susceptibility to atherosclerosis and macrophage recruitment into tissues. *Proc Natl Acad Sci USA* 99(9):6298–6303, PMID: 11972062, <https://doi.org/10.1073/pnas.092327399>.
- Villeneuve DL, Blankenship AL, Giesy JP. 2000. Derivation and application of relative potency estimates based on *in vitro* bioassay results. *Environ Toxicol Chem* 19(11):2835–2843, <https://doi.org/10.1002/etc.5620191131>.
- Wang D, Yan S, Yan J, Teng M, Meng Z, Li R, et al. 2019. Effects of triphenyl phosphate exposure during fetal development on obesity and metabolic dysfunctions in adult mice: impaired lipid metabolism and intestinal dysbiosis. *Environ Pollut* 246:630–638, PMID: 30605818, <https://doi.org/10.1016/j.envpol.2018.12.053>.
- Wang N, Lan D, Chen W, Matsuura F, Tall AR. 2004. ATP-binding cassette transporters G1 and G4 mediate cellular cholesterol efflux to high-density lipoproteins. *Proc Natl Acad Sci USA* 101(26):9774–9779, PMID: 15210959, <https://doi.org/10.1073/pnas.0403506101>.
- Wang N, Silver DL, Costet P, Tall AR. 2000. Specific binding of ApoA-I, enhanced cholesterol efflux and altered plasma membrane morphology in cells expressing ABC1. *J Biol Chem* 275(42):33053–33058, PMID: 10918065, <https://doi.org/10.1074/jbc.M005438200>.
- Wang X, Collins HL, Ranalletta M, Fuki IV, Billheimer JT, Rothblat GH, et al. 2007. Macrophage ABCA1 and ABCG1, but not SR-BI, promote macrophage reverse cholesterol transport *in vivo*. *J Clin Invest* 117(8):2216–2224, PMID: 17657311, <https://doi.org/10.1172/JCI32057>.
- Wei GL, Li DQ, Zhuo MN, Liao YS, Xie ZY, Guo TL, et al. 2015. Organophosphorus flame retardants and plasticizers: sources, occurrence, toxicity and human exposure. *Environ Pollut* 196:29–46, PMID: 25290907, <https://doi.org/10.1016/j.envpol.2014.09.012>.
- WHO (World Health Organization). 2018. The top 10 causes of death. <https://www.who.int/news-room/fact-sheets/detail/the-top-10-causes-of-death> [accessed 30 October 2019].
- Yu XH, Fu YC, Zhang DW, Yin K, Tang CK. 2013. Foam cells in atherosclerosis. *Clin Chim Acta* 424:245–252, PMID: 23782937, <https://doi.org/10.1016/j.cca.2013.06.006>.
- Zhang H, Zhang Z, Nakanishi T, Wan Y, Hiromori Y, Nagase H, et al. 2015. Structure-dependent activity of phthalate esters and phthalate monoesters binding to human constitutive androstane receptor. *Chem Res Toxicol* 28(6):1196–1204, PMID: 25938866, <https://doi.org/10.1021/acs.chemrestox.5b00028>.
- Zhao F, Li Y, Zhang S, Ding M, Hu J. 2019. Association of aryl organophosphate flame retardants triphenyl phosphate and 2-ethylhexyl diphenyl phosphate with human blood triglyceride and total cholesterol levels. *Environ Sci Technol Lett* 9:532–537, <https://doi.org/10.1021/acs.estlett.9b00417>.